Ferromagnetic Weyl Fermions in Two-Dimensional Layered Electride Gd$_2$C

Shuyuan Liu,[1,2] Chongze Wang,[1] Liangliang Liu,[3] Jin-Ho Choi[2], Hyun-Jung Kim[4],
Yu Jia,[3] Chul Hong Park,[5] and Jun-Hyung Cho[1,6,*]

[1]Department of Physics, Research Institute for Natural Science, and Institute for High Pressure at Hanyang University,
Hanyang University, 222 Wangsimni-ro, Seongdong-Ku, Seoul 04763, Republic of Korea
[2]College of Energy, Soochow Institute for Energy and Materials Innovations and Key Laboratory of Advanced Carbon Materials and
Wearable Energy Technologies of Jiangsu Province, Soochow University, Suzhou 215006, China
[3]Key Laboratory for Special Functional Materials of the Ministry of Education, Henan University,
Kaifeng 475004, People's Republic of China
[4]Peter Grünberg Institut and Institute for Advanced Simulation, Forschungszentrum Jülich and JARA, 52425 Jülich, Germany
[5]Department of Physics Education, Pusan National University, Pusan 609-735, Republic of Korea
[6]Asia Pacific Center for Theoretical Physics (APCTP), Pohang-si, Gyeongsangbuk-do 37673, Republic of Korea

Recently, two-dimensional layered electrides have emerged as a new class of materials which possess anionic electrons in the interstitial spaces between cationic layers. Here, based on first-principles calculations, we discover a time-reversal-symmetry-breaking Weyl semimetal phase in a unique two-dimensional layered ferromagnetic (FM) electride Gd$_2$C. It is revealed that the crystal field mixes the interstitial electron states and Gd-5d orbitals near the Fermi energy to form band inversions. Meanwhile, the FM order induces two spinful Weyl nodal lines (WNLs), which are converted into multiple pairs of Weyl nodes through spin-orbit coupling. Further, we not only identify Fermi-arc surface states connecting the Weyl nodes but also predict a large intrinsic anomalous Hall conductivity due to the Berry curvature produced by the gapped WNLs. Our findings demonstrate the existence of Weyl fermions in the room-temperature FM electride Gd$_2$C, therefore offering a new platform to investigate the intriguing interplay between electride materials and magnetic Weyl physics.

In the past decade, two-dimensional (2D) layered materials have attracted tremendous attention because of their promising opportunities in both fundamental research and technological applications [1–4]. Among them, 2D layered electrides [5–8] are highly attractive as a novel class of unconventional ionic compounds, where some excess electrons are confined in the interstitial spaces between positively charged cationic layers. These interstitial electrons behaving as interstitial quasiatoms [9] or anions form a 2D electron gas with exciting electronic properties, such as high electrical conductivities, low work functions, highly anisotropic optical response, and rich surface-related chemical reactions [10–12]. Interestingly, depending on the cationic constituent atoms, interstitial electrons in 2D layered electrides have different degrees of localization to form various electronic phases [13]. For example, the 2D layered electrides of Ca$_2$N [10] and Gd$_2$C [14] which show the features of delocalized and localized interstitial electrons [see Fig. 1(a)] have been experimentally and theoretically demonstrated to exhibit nonmagnetic (NM) and ferromagnetic (FM) phases, respectively.

Because of the loosely bound nature of interstitial electrons away from the cationic layers, 2D layered electrides tend to have the corresponding bands near the Fermi energy E_F [10]. These electronic properties of 2D layered electrides could be favorable for achieving topological phases through band inversions [15,16], which are characterized by the nontrivial topology of bulk bands and
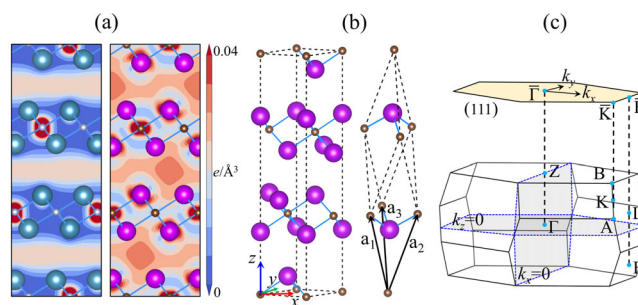

FIG. 1. (a) Calculated partial charge densities of Ca$_2$N (left) and Gd$_2$C (right), (b) optimized structure of Gd$_2$C within the trigonal conventional cell (left) and rhombohedral primitive cell (right), and (c) Brillouin zone of the rhombohedral primitive cell. In (a), each charge density integrated between $E_F - 1.0$ eV and E_F is plotted on the (110) plane of the conventional unit cell. The large and small spheres represent Ca (Gd) cations and N (C) anions, respectively. In (c), the $k_z = 0$ and $k_x = 0$ planes are drawn, and the (111) surface Brillouin zone is also drawn.

its associated robust surface states. The resulting combination between electride property and topological electronic characteristics provides versatile platforms to design electrides with new functionalities that offer great promise in future electronic device applications. Recently, it has been suggested that some 2D layered electrides host nontrivial topological phases such as topological insulators Sc_2C and HfBr as well as nodal-line semimetals Y_2C, Sr_2Bi, and Rb_3O [17–22]. All of these topological phases arising from the NM or paramagnetic electrides limit their tunability and functionality with magnetization. On the other hand, the 2D layered FM electride Gd_2C with a high Curie temperature of ∼350 K [14] is here demonstrated to have a novel quantum state of magnetic Weyl semimetal (WSM), which hosts Weyl fermions in the bulk and unique Fermi-arc surface states connecting pairs of Weyl nodes. Indeed, magnetic WSMs have a variety of novel magnetic responses such as chiral magnetic effects, large anomalous Hall conductivity, and quantum anomalous Hall (QAH) effect [23,24]. In contrast to many inversion symmetry-broken WSMs [25–28], magnetic WSMs with breaking time-reversal symmetry (TRS) have been experimentally realized in only a few ternary nonelectride compounds such as GdPtBi [29], $Y_2Ir_2O_7$ [30], $HgCr_2Se_4$ [31,32], and $Co_3Sn_2S_2$ [33–36]. Therefore, as the first FM WSM electride, Gd_2C is a unique material involving the interplay of electride nature, ferromagnetism, and nontrivial band topology.

In this Letter, using first-principles calculations, we discover a WSM phase in the FM electride Gd_2C that was recently synthesized [14]. This TRS-breaking WSM phase is driven by the combined effects of crystal field, ferromagnetism, and spin-orbital coupling (SOC). We find that the crystal field inverts the hybridized bands of the interstitial electron states and Gd-$5d$ orbitals near E_F, which lead to the formation of band crossings. Meanwhile, the FM order induces spinful Weyl nodal lines (WNLs) having twofold degenerate spin-up or spin-down band crossings along one-dimensional lines in momentum space. Finally, the inclusion of SOC transforms the WNLs into multiple pairs of Weyl nodes. We further demonstrate the existence of topological Fermi-arc states on the (111) surface as well as strong intrinsic anomalous Hall effects due to the large Berry curvature created by the SOC-driven gap openings of WNLs. The present study has important implications for understanding the FM Weyl physics involved in 2D layered electrides such as Gd_2C as well as other isostructural lanthanide carbides Tb_2C and Dy_2C, which will stimulate experimental studies in the future.

We first optimize the structure of Gd_2C using the DFT + U calculation without including SOC [37]. Figures 1(b) and 1(c) show the optimized structure with the lattice parameters $a_1 = a_2 = a_3 = 6.516$ Å and its Brillouin zone, respectively. The calculated spin-up and spin-down bands are displayed in Fig. 2(a). We find that

there are two (four) spinful linear band crossings along the $\overline{LA}$ ($\overline{BZ}$) line around E_F, indicated by circles in Fig. 2(a). The linear crossings along the $\overline{LA}$ line continuously evolve to form three-dimensional (3D) closed-loop shapes of WNLs around the L points [see Fig. 2(d)]. Meanwhile, those along the $\overline{BZ}$ line form two species of WNLs: one is the closed loops around the Z point and the other is the open lines along the k_z direction [see Fig. 2(e)]. It is noted that the spin-up and spin-down bands are decoupled with each other in the absence of SOC. Since the crystalline
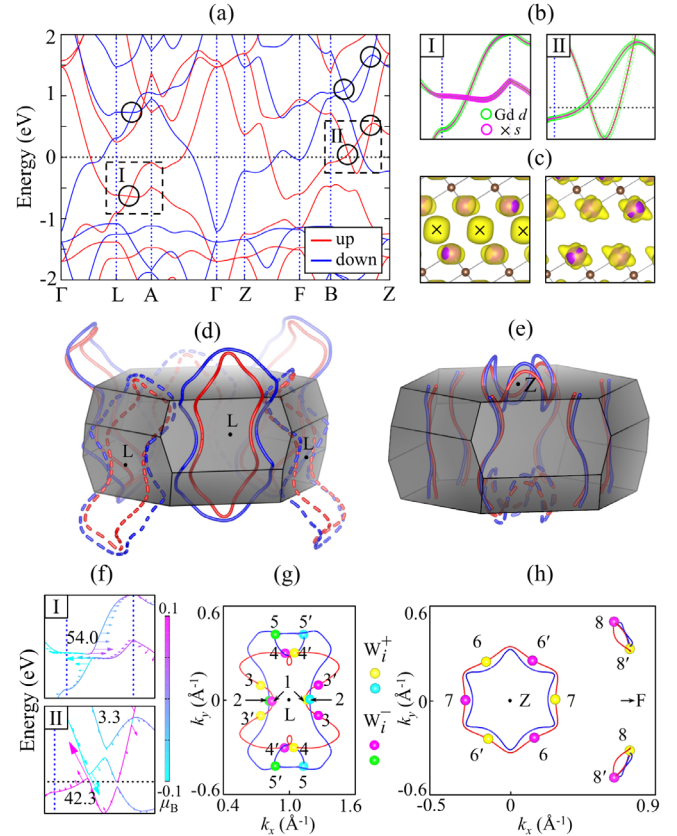

FIG. 2. (a) Calculated band structure of Gd_2C using the DFT + U calculation in the absence of SOC, (b) projected bands onto the Gd-d and interstitial-s-like orbitals in the regions I and II, (c) charge character of the Weyl node in the region I with an isosurface of 0.03 $e/Å^3$, and (d),(e) spinful WNLs. The energy zero in (a) represents E_F. The radii of circles in (b) are proportional to the weights of the corresponding orbitals. The dashed lines in (d) and (e) represent the identical WNLs with modulo the corresponding reciprocal vectors. The closeup band structures in the regions I and II, computed with including SOC, are displayed in (f), where the arrows represent the m_x (horizontal direction) and m_y (vertical direction) components and the arrow colors indicate m_z. The values m_x, m_y, and m_z for the longest arrow in I (II) are −0.252, 0, and −0.123 (−0.187, 0.324, and 2.021) μ_B, respectively. The numbers in (f) represent the SOC-induced gap size in meV. The k_x and k_y positions of the Weyl nodes existing in the energy range between $E_F - 1.0$ and $E_F + 1.0$ eV are drawn in (g) and (h).

symmetries of Gd_2C belong to the space group $R\bar{3}m$ (No. 166) with the point group D_{3d} containing space-inversion symmetry P, threefold rotational symmetry C_{3z} about the z axis, and twofold rotation symmetry C_2 about the y axis and two y' axes (obtained by the $\pm 120°$ rotation of the y axis about the z axis), we find a total of twenty WNLs in the whole Brillouin zone, as shown in Fig. 2(d) and 2(e). To identify the electronic origin of WNLs, we project the crossing bands onto the Gd-$5d$ and interstitial-s-like orbitals [see Fig. 2(b)], which are more dominant components compared to other orbitals (see Fig. S4 in the Supplemental Material [38]). It is thus likely that the band inversions along the $\overline{LA}$ and $\overline{BZ}$ lines are derived from the Gd-$5d$ and interstitial-s-like orbitals. As shown in Fig. 2(c), the charge character of the doubly degenerate Weyl node in the region I represents major distributions at Gd atoms and the interstitial regions ($\times$) between interlayers. It was reported [18] that the NM phase of Y_2C [44] has a closed-loop shape of Dirac nodal lines (DNLs) around the L points with a hybridization of the Y-$4d$ and interstitial-s-like orbitals. Therefore, we can say that the crystal fields of isostructural Y_2C and Gd_2C with the same crystalline symmetries similarly induce band inversions and crossings near E_F, leading to their DNLs and WNLs, respectively.

In contrast to usual nodal lines residing on 2D mirror planes of the Brillouin zone [45], the present WNLs exhibit the 3D snakelike wrapped loops or lines [see Figs. 2(d) and 2(e)]. We note that the DNLs in Y_2C are protected by P symmetry and TRS [18]. Meanwhile, the FM order of Gd_2C breaking TRS produces two spinful WNLs, which are protected by P symmetry. To confirm the symmetry protection of the WNLs, we introduce various displacements of Gd atoms which break or preserve P symmetry. Obviously, our calculated DFT band shows the gap openings of WNLs for the P-symmetry-breaking geometries (see Fig. S5 in the Supplemental Material [38]). We further identify the nontrivial topological characterization of WNLs by calculating the topological index [46], defined as $\zeta_1 = (1/\pi) \oint_c dk \cdot A(k)$, along a closed loop encircling any of the present WNLs. Here, $A(k) = -i\langle u_k | \partial_k | u_k \rangle$ is the Berry connection of the related Bloch bands. We obtain $\zeta_1 = \pm 1$ for the WNLs, indicating that they are stable against the lattice deformations conserving P symmetry.

Next, we calculate the band structure of Gd_2C using the DFT $+ U$ calculation with including SOC. We find that SOC lifts the degeneracy at the band-crossing points along the $\overline{LA}$ and $\overline{BZ}$ lines [see Fig. 2(f)]. Each spin-up (spin-down) WNL around the L points becomes gapped with the exception of five (three) pairs of Weyl nodes, while the two species of spin-up (spin-down) WNLs in Fig. 2(e) are converted into three and two (six and two) pairs of Weyl nodes. Figures 2(g) and 2(h) display the distributions of Weyl nodes within the energy range between $E_F - 1.0$ and $E_F + 1.0$ eV. Since spin is no longer a good quantum number in the presence of SOC, three additional pairs of Weyl nodes between the spin-up and spin-down bands appear around the Z point (see Fig. S6 in the Supplemental Material [38]). We note that the magnitudes of the SOC-driven gaps of WNLs are determined by orbital magnetic moments [see Fig. 2(f)], which are generated by the hybridization of the Gd-$5d$ and interstitial-s-like orbitals [see Fig. 2(b)]. As a consequence of SOC, the spontaneous magnetization points along the z axis, which is more favorable than the magnetization direction along the x axis by 0.12 meV per primitive unit cell (see Table SII in the Supplemental Material [38]). Therefore, the magnetic point group of the system changes into C_{3i} containing P, C_{3z}, and the product C_2T of rotation C_2 and TRS T. As shown in Figs. 2(f) and 2(g), each pair of Weyl nodes associated with inversion P has its counterpart through $C_{2y}T$ symmetry, e.g., (W_3^+, W_3^-) and $(W_{3'}^+, W_{3'}^-)$, while the counterparts of (W_1^+, W_1^-), (W_2^+, W_2^-), and (W_7^+, W_7^-) are themselves. Here, the chiral charge of each Weyl node is determined by calculating the Berry flux through a 2D closed surface enclosing the node. The computed chiral charges (i.e., Chern numbers) have the values of $+1$ and -1 for W_i^+ and W_i^-, respectively. The positions of all twenty-four pairs of Weyl nodes in the Brillouin zone are given in Table SIII of the Supplemental Material [38], together with their energies.

To elucidate the existence of topologically protected surface states that represent the essential hallmark of Weyl nodes, we calculate the surface electronic structure of Gd_2C using the Green's function method based on the tight-binding Hamiltonian with maximally localized Wannier functions [47,48]. Figure 3(a) shows the projected surface spectrum for the (111) surface of Gd_2C. We find topological surface states around the $\bar{K}$ and $\bar{K}'$ points near E_F. Such nontrivial surface states can be more distinguishable by subtracting the (111) projected bulk states from the surface spectrum (see Fig. S7 in the Supplemental Material [38]). In Fig. 3(b), we plot the Fermi surface of the (111) surface at a chemical potential of 0.06 eV above E_F. It is obviously seen that there are open Fermi arcs connecting $W_8^+(W_{8'}^+)$ and $W_{8'}^-$ (W_8^-) around the $\bar{K}$ $(\bar{K}')$ point. Furthermore, these topological surface states are spin polarized with helical spin textures [see the insets in Fig. 3(b)], reflecting a unique spin-momentum locking property in topological surface states [49]. Figure 3(c) also shows the topological surface states connecting W_1^+ and W_1^- around the $\bar{F}$ point. Interestingly, the Fermi surface at a chemical potential of -0.90 eV below E_F exhibits two Fermi arcs connecting the W_1^+ and W_1^- nodes, similar to the drumheadlike surface states obtained without including SOC (see Fig. S8 of the Supplemental Material [38]). This tiny variation of topological surface states in the presence of SOC is likely caused by small energy gap openings along the WNL connecting W_1^+ and W_1^-.
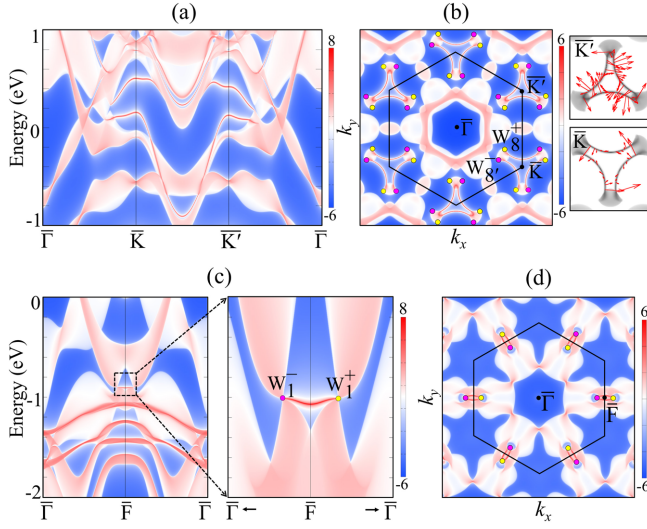
FIG. 3. (a) Projected surface spectrum for the (111) surface of Gd_2C with (b) the isoenergy surface at 0.06 eV above E_F. The in-plane spin textures of the surface states around the $\bar{K}$ and $\bar{K}'$ points are also drawn in (b). Another projected surface spectrum along the $\bar{\Gamma}$-$\bar{F}$-$\bar{\Gamma}$ and the isoenergy surface at −0.90 eV below E_F are displayed in (c) and (d), respectively. A closeup image around the $\bar{F}$ point is given in (c).

The search for room-temperature magnetic WSM materials has lately been very demanding of attention because of their novel magnetic responses that may be used for future spintronics technologies [34,36,50]. In order to estimate the Curie temperature T_c of Gd_2C, we perform spin-polarized calculations for the FM and three different antiferromagnetic (AFM) configurations (see Fig. S9 in the Supplemental Material [38]). The FM configuration is found to be more stable than the lowest-energy AFM configuration by 48.6 meV per Gd atom. For the FM configuration, the magnetic moment of Gd_2C is found to originate predominantly from the Gd $4f$ orbitals (see Table SIV in the Supplemental Material [38]). Using the mean field approximation [51], we estimate a T_c of ∼377 K, in good agreement with the experimental value of $T_c \approx 350$ K [14]. The resulting room-temperature FM WSM phase is expected to exhibit the intrinsic anomalous Hall effect originating from Berry curvature. Figure 4(a) shows the energy-dependent anomalous Hall conductivity σ_{xy} calculated by integrating the Berry curvature along k_z in the Brillouin zone. We find that σ_{xy} is 399 Ω^{-1} cm^{-1} at E_F, while it shows a large peak of ∼1167 Ω^{-1} cm^{-1} at 0.06 eV above E_F. It is thus likely that an electron doping of ∼0.07e per primitive unit cell shifting E_F to 0.06 eV (see Fig. S10 in the Supplemental Material [38]) could increase σ_{xy} significantly. Figures 4(b) and 4(c) show the Berry curvature distributions in the $k_z = 0$ and $k_x = 0$ planes [see Fig. 1(c)], respectively. We find that there are hot spots of the Berry curvature, originating from the gapped WNLs around W_8, W_{13}, and W_{14} (see Table SIII in the Supplemental Material [38]). Such intrinsic Berry curvature
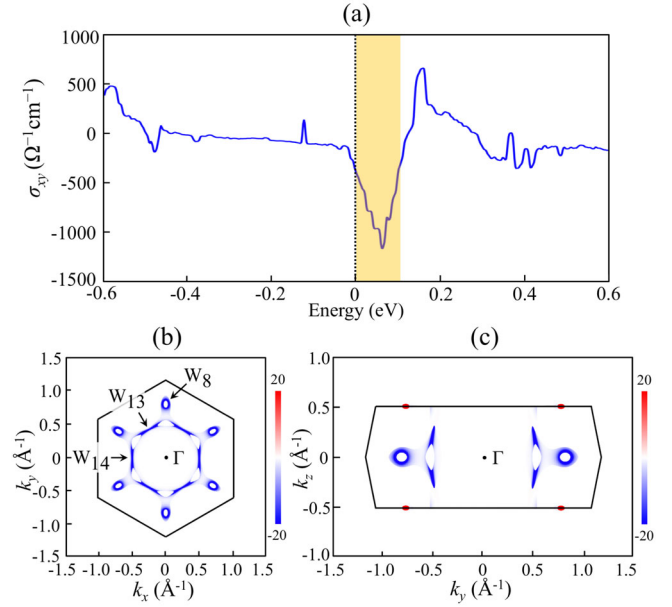

FIG. 4. (a) Energy dependence of the anomalous Hall conductivity σ_{xy} and Berry curvature distribution in (b) the $k_z = 0$ plane and (c) the $k_x = 0$ plane of the Brillouin zone [see Fig. 1(c)]. In (b) and (c), the z component of Berry curvature is integrated between E_F and $E_F + 0.1$ eV [see the yellow colored region in (a)], and the red and blue regions indicate positive and negative values of Berry curvature, respectively.

gives rise to the large peak of σ_{xy} that is a fascinating electronic transport behavior.

To conclude, based on first-principles calculations, we have discovered the emergence of a WSM phase in a 2D layered FM electride material Gd_2C. We revealed that this TRS-breaking WSM phase is driven by the combined effects of crystal field, ferromagnetism, and SOC. The crystal field inverts the hybridized bands of the interstitial electron states and Gd-5d orbitals near E_F, and the FM order induces two spinful WNLs with the shapes of 3D snakelike wrapped loops and lines. Finally, SOC splits the WNLs into multiple pairs of Weyl nodes with opposite chirality. We further demonstrated not only Fermi-arc surface states connecting the Weyl nodes but also large intrinsic anomalous Hall conductivity originating from the Berry curvature created by the gapped WNLs. It is note-worthy that other isostructural lanthanide carbides such as Tb_2C and Dy_2C also show similar band dispersions and band crossings near E_F (see Fig. S11 in the Supplemental Material [38]), thereby hosting magnetic WSM phases. Therefore, our results not only establish the intriguing interplay of electride properties, ferromagnetism, and non-trivial Weyl band topology in Gd_2C, but also open the door for the emergence of topological WSM phase in 2D layered FM lanthanide carbides. Finally, we note that the QAH effect may emerge in the 2D limit of magnetic WSMs due to finite-size effects in thin films [52]. However, our DFT + U calculation shows that monolayer Gd_2C is

unlikely to be transformed into a QAH insulator, due to the presence of electronic states crossing E_F (see Fig. S12 in the Supplemental Material [38]). We anticipate a high-throughput computational search for magnetic electrides with Weyl fermions in the future by using recently developed screening schemes [53,54] which were employed to search for various electrides containing topological phases such as topological insulator, topological crystalline insulator, and high-symmetry point semimetal.

S. L. and C. W. contributed equally to this work.

―――――――――

*Corresponding author.
chojh@hanyang.ac.kr

[1] K. S. Novoselov, A. K. Geim, S. V. Morozov, D. Jiang, Y. Zhang, S. V. Dubonos, I. V. Grigorieva, and A. A. Firsov, Science **306,** 666 (2004).

[2] A. H. Castro Neto, F. Guinea, N. M. R. Peres, K. S. Novoselov, and A. K. Geim, Rev. Mod. Phys. **81,** 109 (2009).

[3] W. Choi, N. Choudhary, G. H. Han, J. Park, D. Akinwande, and Y. H. Lee, Mater. Today **20,** 116 (2017).

[4] K. S. Novoselov, A. Mishchenko, A. Carvalho, and A. H. Castro Neto, Science **353,** aac9439 (2016).

[5] T. Inoshita, S. Jeong, N. Hamada, and H. Hosono, Phys. Rev. X **4,** 031023 (2014).

[6] X. Zhang, Z. Xiao, H. Lei, Y. Toda, S. Matsuishi, T. Kamiya, S. Ueda, and H. Hosono, Chem. Mater. **26,** 6638 (2014).

[7] W. Ming, M. Yoon, M. H. Du, K. Lee, and S. W. Kim, J. Am. Chem. Soc. **138,** 15336 (2016).

[8] S. Yi, J.-H. Choi, K. Lee, S. W. Kim, C. H. Park, and J.-H. Cho, Phys. Rev. B **94,** 235428 (2016).

[9] M. Miao and R. Hoffman, J. Am. Chem. Soc. **137,** 3631 (2015).

[10] K. Lee, S. W. Kim, Y. Toda, S. Matsuishi, and H. Hosono, Nature (London) **494,** 336 (2013).

[11] J. L. Dye, Science **301,** 607 (2003).

[12] M. Kitano, Y. Inoue, Y. Yamazaki, F. Hayashi, S. Kanbara, S. Matsuishi, T. Yokoyama, S. Kim, M. Hara, and H. Hosono, Nat. Chem. **4,** 934 (2012).

[13] S. Liu, W. Li, S. W. Kim, and J.-H. Choi, J. Phys. Chem. C **124,** 1398 (2020).

[14] S. Y. Lee, J.-Y. Hwang, J. Park, C. N. Nandadasa, Y. Kim, J. Bang, K. Lee, K. H. Lee, Y. Zhang, Y. Ma, H. Hosono, Y. H. Lee, S.-G. Kim, and S. W. Kim, Nat. Commun. **11,** 1526 (2020).

[15] B. Bradlyn, L. Elcoro, J. Cano, M. G. Vergniory, Z. Wang, C. Felser, M. I. Aroyo, and B. A. Bernevig, Nature (London) **547,** 298 (2017).

[16] H. C. Po, A. Vishwanath, and H. Watanabe, Nat. Commun. **8,** 50 (2017).

[17] M. Hirayama, S. Matsuishi, H. Hosono, and S. Murakami, Phys. Rev. X **8,** 031067 (2018).

[18] H. Huang, K.-H. Jin, S. Zhang, and F. Liu, Nano Lett. **18,** 1972 (2018).

[19] L. Liu, C. Wang, S. Yi, D. K. Kim, C. H. Park, and J.-H. Cho, Phys. Rev. B **99,** 220401(R) (2019).

[20] S.-C. Zhu, L. Wang, J.-Y. Qu, J.-J. Wang, T. Frolov, X.-Q. Chen, and Q. Zhu, Phys. Rev. Mater. **3,** 024205 (2019).

[21] X. Zhang, B. Fu, L. Jin, X. Dai, G. Liu, and Y. Yao, J. Phys. Chem. C **123,** 25871 (2019).

[22] C. Park, S. W. Kim, and M. Yoon, Phys. Rev. Lett. **120,** 026401 (2018).

[23] D. Kurebayashi and K. Nomura, Phys. Rev. Applied **6,** 044013 (2016).

[24] Y. Tokura, M. Kawasaki, and Naoto Nagaosa, Nat. Phys. **13,** 1056 (2017).

[25] H. Weng, C. Fang, Z. Fang, B. A. Bernevig, and X. Dai, Phys. Rev. X **5,** 011029 (2015).

[26] L. X. Yang, Z. K. Liu, Y. Sun, H. Peng, H. F. Yang, T. Zhang, B. Zhou, Y. Zhang, Y. F. Guo, M. Rahn *et al.*, Nat. Phys. **11,** 728 (2015).

[27] A. A. Soluyanov, D. Gresch, Z. Wang, Q. Wu, M. Troyer, X. Dai, and B. A. Bernevig, Nature (London) **527,** 495 (2015).

[28] A. Tamai, Q. S. Wu, I. Cucchi, F. Y. Bruno, S. Riccó, T. K. Kim, M. Hoesch, C. Barreteau, E. Giannini, C. Besnard, A. A. Soluyanov, and F. Baumberger, Phys. Rev. X **6,** 031021 (2016).

[29] T. Suzuki, R. Chisnell, A. Devarakonda, Y.-T. Liu, W. Feng, D. Xiao, J. W. Lynn, and J. G. Checkelsky, Nat. Phys. **12,** 1119 (2016).

[30] X. Wan, A. M. Turner, A. Vishwanath, and S. Y. Savrasov, Phys. Rev. B **83,** 205101 (2011).

[31] G. Xu, H. Weng, Z. Wang, X. Dai, and Z. Fang, Phys. Rev. Lett. **107,** 186806 (2011).

[32] S. Yang, Z. Li, C. Lin, C. Yi, Y. Shi, D. Culcer, and Y. Li, Phys. Rev. Lett. **123,** 096601 (2019).

[33] E. Liu, Y. Sun, N. Kumar, L. Muechler, A. Sun, L. Jiao, S.-Y. Yang, D. Liu, A. Liang, Qiunan Xu *et al.*, Nat. Phys. **14,** 1125 (2018).

[34] D. F. Liu, A. J. Liang, E. K. Liu, Q. N. Xu, Y. W. Li, C. Chen, D. Pei, W. J. Shi, S. K. Mo, P. Dudin, T. Kim, C. Cacho, G. Li, Y. Sun, L. X. Yang, Z. K. Liu, S. S. P. Parkin, C. Felser, and Y. L. Chen, Science **365,** 1282 (2019).

[35] J.-X. Yin, S. S. Zhang, G. Chang, Q. Wang, S. S. Tsirkin, Z. Guguchia, B. Lian, H. Zhou, K. Jiang, I. Belopolski, N. Shumiya, D. Multer, M. Litskevich, T. A. Cochran, H. Lin, Z. Wang, T. Neupert, S. Jia, H. Lei, and M. Z. Hasan, Nat. Phys. **15,** 443 (2019).

[36] N. Morali, R. Batabyal, P. K. Nag, E. Liu, Q. Xu, Y. Sun, B. Yan, C. Felser, N. Avraham, and H. Beidenkopf, Science **365,** 1286 (2019).

[37] The present density-functional theory (DFT) calculations were performed using the Vienna *ab initio* simulation package with the projector-augmented wave (PAW) method [55–57]. For the exchange-correlation energy, we employed

the generalized-gradient approximation functional of Perdew, Burke, and Ernzerhof [58]. We performed the DFT + U calculation using the Dudarevs approach [59], with the Hubbard parameter $U = 6.7$ eV and exchange interaction parameter $J = 0.7$ eV. We note that, although the variation of the effective U value, $U_{\text{eff}} = U - J$, significantly changes the positions of Gd $4f$ states, the band topology of the hybridized states of interstitial-s-like and Gd-$5d$ orbitals around E_F is not influenced by the presence or absence of U_{eff} (see Fig. S1 in the Supplemental Material [38]). Therefore, the topological features near E_F remain intact with respect to U_{eff}. In order to examine the validity of the Dudarev's approach which has a simplified form of the on-site Hubbard-like interaction (E_{Hub}) and double counting (E_{DC}) terms, we performed an additional DFT + U calculation with the Liechtenstein's approach [60] where U and J are separately included to more rigorously consider E_{Hub} and E_{DC} from the Hartree-Fock method. We find that the band structures of Gd_2C obtained using the two approaches are almost the same as each other, as shown in Fig. S2 in the Supplemental Material [38]. For bulk Gd_2C, the adjacent three Gd_2C layers are stacked in an ABC-type trilayer pattern along the z direction, as shown in Fig. 1(b). A plane wave basis was employed with a kinetic energy cutoff of 550 eV, and the k-space integration was done with and $21 \times 21 \times 21$ meshes in the Brillouin zone. All atoms were allowed to relax along the calculated forces until all the residual force components were less than 0.01 eV/Å. It is noteworthy that the inclusion of van der Waals interactions hardly influences the lattice parameters, band structure, and magnetic moment of Gd_2C (see Table SI and Fig. S3 in the Supplemental Material [38]).

[38] See Supplemental Material at http://link.aps.org/supplemental/10.1103/PhysRevLett.125.187203 for the DFT + U methods, the vdW-corrected bands, the orbital-projected band structure of bulk Gd_2C, the band structure of the P-symmetry-breaking geometry, the difference between the surface and bulk spectra of the Gd_2C (111) surface, the drumhead-like surface state in the absence of SOC, the estimation of Curie temperature, the band structures and WNLs of bulk Tb_2C and Dy_2C, the magnetic anisotropic energy of bulk Gd_2C, and the positions and energies of Weyl nodes, which includes Refs. [39–43].

[39] S. Grimme, J. Antony, S. Ehrlich, and S. Krieg, J. Chem. Phys. **132**, 154104 (2010).

[40] S. Grimme, S. Ehrlich, and L. Goerigk, J. Comput. Chem. **32**, 1456 (2011).

[41] J. Klimeš, D. R. Bowler, and A. Michaelides, J. Phys. Condens. Matter **22**, 022201 (2010).

[42] M. Dion, H. Rydberg, E. Schröder, D. C. Langreth, and B. I. Lundqvist, Phys. Rev. Lett. **92**, 246401 (2004).

[43] Y. Mudryk, Durga Paudyal, V. K. Pecharsky, and K. A. Gschneidner, J. Appl. Phys. **109**, 07A924 (2011).

[44] We note that the DNLs are based on a nonmagnetic phase. However, most of experimental [61–64] and theoretical [19,65] studies of Y_2C reported the existence of a paramagnetic or a weak ferromagnetic phase.

[45] R. Li, H. Ma, X. Cheng, S. Wang, D. Li, Z. Zhang, Y. Li, and X.-Q. Chen, Phys. Rev. Lett. **117**, 096401 (2016).

[46] C. Fang, H. Weng, X. Dai, and Z. Fang, Chin. Phys. B **25**, 117106 (2016).

[47] A. A. Mostofi, J. R. Yates, Y.-S. Lee, I. Souza, D. Vanderbilt, and N. Marzari, Comput. Phys. Commun. **178**, 685 (2008).

[48] Q. S. Wu, S. N. Zhang, H.-F. Song, M. Troyer, and A. A. Soluyanov, Comput. Phys. Commun. **224**, 405 (2018).

[49] X.-Q. Sun, S.-C. Zhang, and Z. Wang, Phys. Rev. Lett. **115**, 076802 (2015).

[50] I. Belopolski *et al.*, Science **365**, 1278 (2019).

[51] G. S. Rushbrooke and P. J. Wood, Mol. Phys. **1**, 257 (1958); **6**, 409 (1963).

[52] L. Muechler, E. Liu, J. Gayles, Q. Xu, C. Felser, and Y. Sun, Phys. Rev. B **101**, 115106 (2020).

[53] L. A. Burton, F. Ricci, W. Chen, G.-M. Rignanese, and G. Hautier, Chem. Mater. **30**, 7521 (2018).

[54] Q. Zhu, T. Frolov, and K. Choudhary, Matter **1**, 1293 (2019).

[55] G. Kresse and J. Hafner, Phys. Rev. B **48**, 13115 (1993).

[56] G. Kresse and J. Furthmüller, Comput. Mater. Sci. **6**, 15 (1996).

[57] P. E. Blöchl, Phys. Rev. B **50**, 17953 (1994).

[58] J. P. Perdew, K. Burke, and M. Ernzerhof, Phys. Rev. Lett. **77**, 3865 (1996); **78**, 1396 (1997).

[59] S. L. Dudarev, G. A. Botton, S. Y. Savrasov, C. J. Humphreys, and A. P. Sutton, Phys. Rev. B **57**, 1505 (1998).

[60] A. I. Liechtenstein, V. I. Anisimov, and J. Zaanen, Phys. Rev. B **52**, R5467 (1995).

[61] J. Park, K. Lee, S. Y. Lee, C. N. Nandadasa, S. Kim, K. H. Lee, Y. H. Lee, H. Hosono, S.-G. Kim, and S. W. Kim, J. Am. Chem. Soc. **139**, 615 (2017).

[62] X. Zhang, Z. Xiao, H. Lei, Y. Toda, S. Matsuishi, T. Kamiya, S. Ueda, and H. Hosono, Chem. Mater. **26**, 6638 (2014).

[63] S. Otani, K. Hirata, Y. Adachi, and N. Ohashi, J. Cryst. Growth **454**, 15 (2016).

[64] M. Hiraishi, K. M. Kojima, I. Yamauchi, H. Okabe, S. Takeshita, A. Koda, R. Kadono, X. Zhang, S. Matsuishi, H. Hosono, K. Hirata, S. Otani, and N. Ohashi, Phys. Rev. B **98**, 041104(R) (2018).

[65] T. Inoshita, N. Hamada, and H. Hosono, Phys. Rev. B **92**, 201109(R) (2015).